Journal of
Synchrotron
Radiation

ISSN 0909-0495

Received 18 January 2011
Accepted 4 August 2011

Design and construction of multicrystal analyser detectors using Rowland circles: application to MAD26 at ALBA

Inma Peral,[a]* Jonathan McKinlay,[b] Michael Knapp[a] and Salvador Ferrer[a]

[a]ALBA-CELLS, Carretera, BP 1413, Km. 3.3, E-08290 Cerdanyola, Barcelona, Spain, and [b]Australian Synchrotron, 800 Blackburn Road, Clayton, VIC 3168, Australia. E-mail: iperal@cells.es

A concept is given for describing multicrystal analyser detectors (MADs), as they are in use for synchrotron powder diffraction, on the basis of the Rowland circle construction. The Rowland circle is typically used to describe focusing geometries and can be adapted for the case of MADs working at a single energy as well as in a limited energy range. With this construction it is also possible to quantify and optimize the walk of the beam along non-central crystals which is inevitable in certain detector designs. The results of this geometrical inspection are correlated with a real detector design that is implemented at the ALBA synchrotron facility in Spain. An error budget is given to estimate the influence and amount of tolerance of the manufacturing process.

Keywords: high-resolution powder diffraction; multicrystal analyser detectors; synchrotron; error budget; Rowland circle; Johansson monochromator.

1. Introduction

The last few decades of the 20th century transformed the powder diffraction method from a technique familiar to a few into one of the most broadly practicable analytical diffraction experiments. Nowadays powder diffraction is the workhorse of materials science research.

Besides the beamline optics (or laboratory diffractometer optics), the photon detection system is the most essential component of the experimental set-up and a detector using crystal analysers is considered the best choice for obtaining high-quality powder diffraction data with high angular resolution and low background intensities (Hastings *et al.*, 1984; Cox, 1992; Parrish & Hart, 1985, 1987). The limiting factor in this technique is the amount of time necessary to measure a full pattern, which led to the situation that this set-up is almost only applied in synchrotron facilities (Toraya, 2009).

A considerable reduction in measuring time can be achieved by using compact multicrystal analyser detectors (MADs). Their design is based on a parallel arrangement of a number of individual crystal analysers (about ten) coupled with the corresponding number of point detectors (Toraya *et al.*, 1996; Hodeau *et al.*, 1998). MADs have proven their efficiency to acquire low-background and high-resolution data in synchrotron radiation sources during the last 15 years. During that time a lot of effort has been devoted to developing and optimizing MAD designs in many synchrotron facilities around the world, and today almost every facility has at least one MAD system in operation resulting in a large variety of different designs.

Another main characteristic of MAD designs is the angular offset between individual consecutive crystals. The different layouts range from $\sim 1^\circ$ offset between six channels in the model developed at SNBL (ESRF, France, http://www.esrf.eu/UsersAndScience/Experiments/CRG/BM01/) with the smallest offset, passing through the design by Hodeau *et al.* (1998) with 2° offset between nine channels, to a 12-crystal MAD where all crystals can be independently adjusted by motors in two axes and that is currently in operation at the APS (Chicago, USA) (Lee *et al.*, 2008). Installing several MAD systems on a single diffractometer to further increase throughput has been carried out at Diamond (UK) (Tartoni *et al.*, 2008; Thompson *et al.*, 2009; Parker *et al.*, 2011).

In this paper we describe a new compact X-ray detector based on a multicrystal analyser design developed for high-resolution powder diffraction at the ALBA synchrotron facility, the MAD26, that will be applicable in the energy range between 8 and 50 keV.

2. MAD general description

The MAD26 design is inspired by Hodeau's publication (Hodeau *et al.*, 1998) and follows the same principles. The detector comprises a two-circle goniometer (θ_c–$2\theta_c$) with crystals stacked with an angular offset α between each other. The whole assembly is then mounted on a three-circle diffractometer. The two main differences between Hodeau's design and the MAD26 are (i) the positions of the MAD26 crystals are optimized to minimize the beam walk for a given energy range, and (ii) the MAD26 contains two sets of crystals

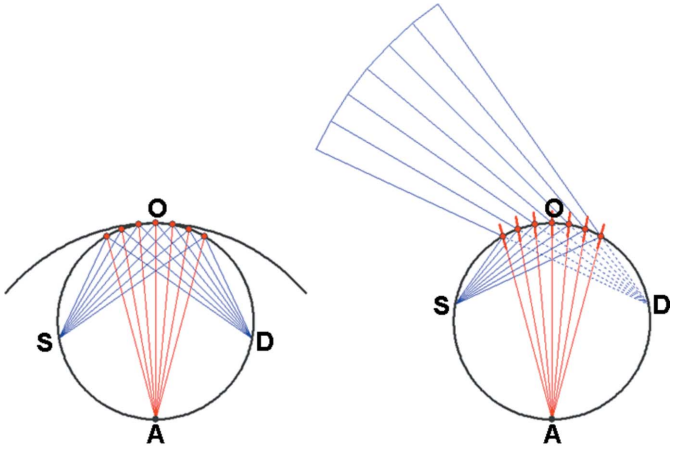

(*a*) (*b*)

Figure 1
(*a*) Bent and ground Johansson monochromator. The outer arc represents the bent lattice planes of the monochromator crystal (the curvature centre is *A* and the radius is 2*R*, where *R* is the radius of the Rowland circle, shown by the black circumference). The Rowland circle lies on the surface of the ground crystal. The red dots represent $2n + 1$ surface points distributed on a 'crystal fan' with a constant angular offset. (*b*) The $2n + 1$ discrete crystals have been rotated (see text). In both (*a*) and (*b*) the central crystal *O*, the source *S* and the focus point *D* are shown.

(Si 111 and Si 220) that can easily be exchanged by means of a linear translation.

2.1. Design principle of the single-energy MAD

At first sight it would not seem obvious to apply the principle of the concave Rowland grating (Rowland, 1902) to fast-acquisition high-resolution powder diffraction, or, what is the same, to MADs. However, it is possible to construct a MAD from the discretization of the Johansson monochromator geometry (Johansson, 1933; Witz, 1969; Caciuffo *et al.*, 1987).

Let us assume an ideal 'breaking' of a bent and ground Johansson monochromator crystal into $2n + 1$ flat pieces (see Fig. 1*a*). These small analyser crystals shall be distributed over a crystal fan with a constant offset between each other. The impinging point of the diffracted beam on each of the crystals will be given by the corresponding points defined by the Johansson construction as seen in the figure (red dots). For practical reasons we want to have the detectors on the upper part of the figure outside the Rowland circle, which means that the crystals have to be rotated clockwise around the impinging point by 90°. Point *D* then acts as a virtual source point (as can be seen in Fig. 1*b*). Once the specific type of analyser crystal is defined and the energy chosen, *i.e.* the Bragg angle is defined, it is always possible to find the Rowland circle on which the source, the virtual focus and the impact points on the crystal surfaces lie. The chord *SO* in Fig. 1 is the distance between the sample and the centre of the crystal analyser stage, and *OA* lies on the central crystal surface or on the normal to the central crystal surface, in Figs. 1(*a*) and 1(*b*), respectively. The radius of the Rowland circle, *R*, and the distance *SO* must fulfil the following condition, $SO = 2R\cos\theta$ [note that in the case of the original Johansson monochromator geometry, Fig. 1(*a*), the condition is $SO = 2R\sin\theta$ owing to the 90° rotation (Witz, 1969, and references therein)].

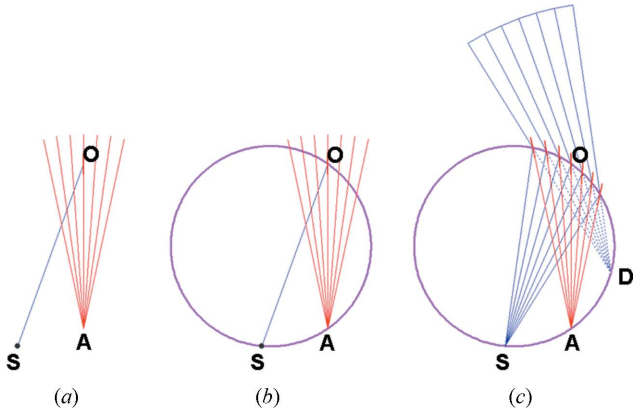

(*a*) (*b*) (*c*)

Figure 2
Construction of the Rowland circle from the points *S*, *O*, *A* and *D*. The lengths of the chords *SO* and *OA* do not need to be the same.

Note that this geometric construction works in a more general case: there is in principle no restriction to the distances *SO* and *OA* or *SO* and *OD*. However, once two of the three distances are fixed, the third is determined by the geometric construction [see, for example, Figs. 2(*a*)–2(*c*) where *SO* is not equal to *OD*]. In fact, Hodeau's design (Fig. 3) fits into this description: it corresponds to the special case where the distance *SO* is approximately equal to distance *OA* and the angular offset between two consecutive crystals is a small angle of 2°. Fig. 4 corresponds to the superposition of Fig. 5(*a*) in Hodeau's publication (Hodeau *et al.*, 1998), showing the configuration of the MAD device at 6 keV superimposed with the Rowland circle, the crystal fan and the virtual source. The centre of the analyser goniometer corresponds to *O*, the *SO* distance corresponds to *D* in Fig. 3, and $d \simeq D\tan\alpha$, where α is the offset angle. Note that, according to the article, d = 14.8 mm $\simeq D\tan\alpha$ = 425 tan(2°) = 14.84 mm.

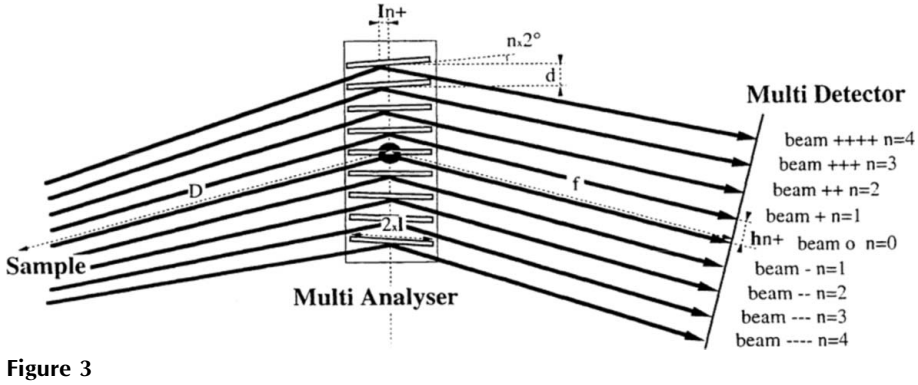

Figure 3
Arrangement of crystals in Hodeau's original paper. Some of the crystals are slightly offset from the support axis to reduce the beam walk.

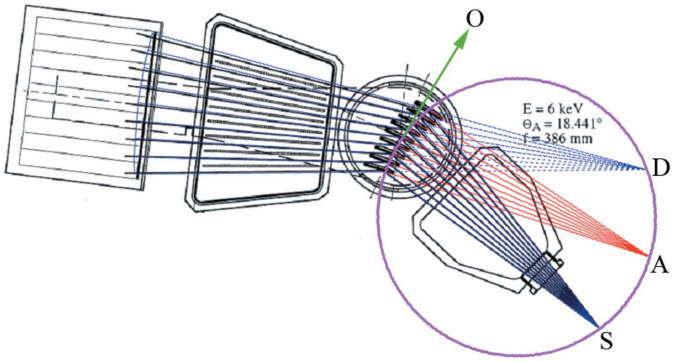

Figure 4
Correspondence between Hodeau's detector at 6 keV and the Rowland construction presented in the text.

2.2. Design principle of the wide-energy-range MAD

The description above only holds for a single energy. Since it is usually the case that multi-crystal analyser detectors at synchrotron beamlines have to work over a wide energy range, the crystal fan must be rotated around O to adjust for the different incoming energies. The energy range, typically an interval $[E_{\rm min}, E_{\rm max}]$ where $E_{\rm min}$ is the minimum energy and $E_{\rm max}$ is the maximum energy, defines the Bragg angle range of the analyser crystal, $\theta_{\rm o} \leq \theta \leq \theta_{\rm f}$ where $0 < \theta < \pi/2$, $E_{\rm min} = 12.3984/(2d\sin\theta_{\rm f})$ and $E_{\rm max} = 12.3984/(2d\sin\theta_{\rm o})$ with $E_{\rm max,\,min}$ given in keV and the lattice spacing of the crystal analyser, d, in Å. Each energy defines a distinct Rowland circle with slightly different radius. Owing to the lever arm, for the non-central crystals the impinging point will move along the surface of the outer crystals (beam walk on the crystal surfaces). The rotation of the crystal stage with energy around its centre at O can alternatively be described as a movement of the sample S along the Rowland circle thereby changing the angle of the fan of rays as well as the distance SO. As a consequence, the virtual source of the rays in D also has to move. Since in the real set-up the distance between sample and centre of the stage, SO, is fixed, the trajectory of the sample movement will lie on a circle with radius SO around O. For each energy the Rowland circle is then defined as the circle passing through A, S and O. The radius of the Rowland circle at a given energy (or θ) can be obtained by calculating the circumradius defined by A, S and O using equation (1) obtained from the circumradius formula by Weisstein (2003),

$$R_\theta = \frac{1}{2}\left[\left(\frac{OA\cos\theta - SO}{\sin\theta}\right)^2 + OA^2,\right]^{1/2}, \qquad (1)$$

where θ, the Bragg angle of the analyser crystal, also corresponds to the angle formed by SO and OA.

The centre of the Rowland circle, C_θ, can be described as the coordinates of the vector $\mathbf{r}_{{\rm ce},\theta}$; the expression is given in equation (2) (Weisstein, 2003) assuming that (i) the reference system is a Cartesian system with x as horizontal axis, y as vertical axis and the origin at O (see Fig. 5*a*), and (ii) for clarity, we assume that the change in energy is described by

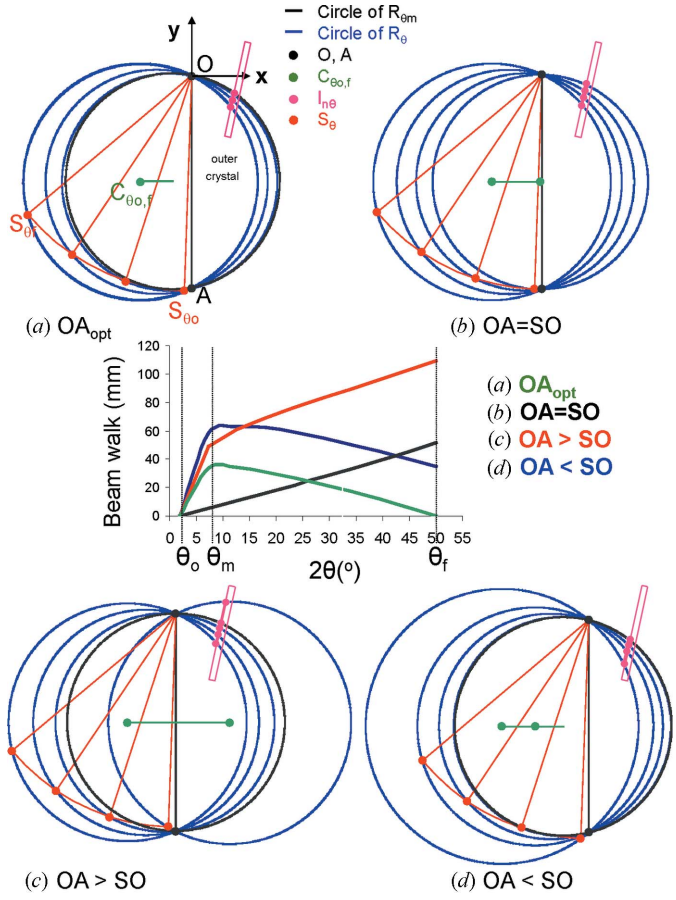

Figure 5
The beam walk on a non-central crystal is shown for the four possible cases: (*a*) $OA = OA_{\rm opt}$, (*b*) $OA = SO$, (*c*) $OA > SO$, and (*d*) $OA < SO$. While the chord SO refers to the central crystal, the beam walk on an outer crystal is given in pink. It is represented by the distance between the impact points on the crystal surface for the operational angles of the detector $\theta_{\rm o} \leq \theta \leq \theta_{\rm f}$ (thick pink line on crystal surface). The minimum, maximum and two intermediate θ angles are shown with the four corresponding Rowland circles (blue circles with the points S, O and A are shown) and the impact points on the non-central crystal ($I_{n\theta}$, pink dots). The centre of the Rowland circle is represented by a green dot (for $\theta_{\rm o}$ and $\theta_{\rm f}$) and the green line depicts its movement over the complete θ range. The non-central crystal is represented by a pink rectangle. The Rowland circle of $\theta_{\rm m}$ is represented by a black circle. The central inset shows the beam walk in millimetres *versus* θ for the four cases. The minimum and maximum Bragg angles $\theta_{\rm o}$ and $\theta_{\rm f}$ as well as $\theta_{\rm m}$ are labelled.

rotating the sample S with respect to O (centre of the crystal stage),

$$\mathbf{r}_{{\rm ce},\theta} = \left[\frac{OA\cos\theta - SO}{2\sin\theta}, \frac{-OA}{2}\right]. \qquad (2)$$

The function of the Rowland radius $\mathbf{r}_{{\rm ce},\theta}$ *versus* energy (or θ) is continuous with only one minimum, $R_{\rm min} = SO/2$ for $\theta_{\rm m} = \arccos(SO/OA)$ if $OA > SO$ or for $\theta_{\rm m} = \arccos(OA/SO)$ if $OA < SO$. In the special case where $SO = OA$, the Rowland radius increases with θ.

The beam walk, bw, is the distance between impinging points on the crystal surface at different energies; these impinging points will be noted as In_θ. The coordinates of the intersection point between the crystal surface of crystal 'n' and

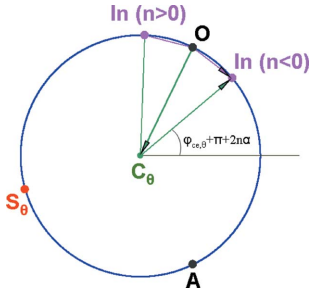

Figure 6
Rowland circle at a given energy (or θ) where A, O, S_θ as well as the impact point I_n and the centre of the Rowland circle C_θ are shown. The angle formed by $\mathbf{rIn}_\theta$ and the x-axis is also indicated.

the beam at a given energy (or θ) are defined by the vector $\mathbf{rIn}_\theta$ where each vector can be calculated using the following expression,

$$\mathbf{rIn}_\theta = \mathbf{r}_{ce,\theta} + R_\theta\left[\cos\left(\varphi_{ce,\theta} + \pi + 2n\alpha\right), \sin\left(\varphi_{ce,\theta} + \pi + 2n\alpha\right)\right], \tag{3}$$

where $\varphi_{ce,\theta}$ is the angle formed by the x-axis and $\mathbf{r}_{ce,\theta}$ (see Fig. 6). The beam walk for two given energies (or angles, θ and θ_1) can then be expressed as the distance between these vectors,

$$bw_{\theta,\theta_1} = \left|\mathbf{rIn}_\theta - \mathbf{rIn}_{\theta_1}\right|. \tag{4}$$

The beam walk is one of the key parameters in the MAD design since it quantifies the displacement of the diffracted beam along the analyser crystal surface with energy. As a consequence, the diffracted beam could be clipped by collimators, slits or neighbouring crystals, thereby deteriorating the diffracted signal. The larger the beam walk, then the larger the crystals should be, which has an important impact on the cost and on the level of complexity of the mechanical design of the MAD. Therefore, it is important to minimize the beam walk over the θ range, and all MAD designs address this point. One common approach is to choose α as a small angle, since it has a direct impact on the amount of beam walk. In Hodeau's design, analytical calculations and X-ray tracing of the beam impact along the analyser crystals are the basis for optimizing the crystal positions. The crystals are not located in the centre line of the comb, as seen in Fig. 3, but in a slightly offset position such that the beam will always hit the crystals for a given energy range. This strategy is ideal in terms of maintaining the reflected beams centrally on the analyser crystals and detectors; besides, the analytical calculations provide a valuable tool to optimize the position of the crystals and to minimize the beam walk. However, the optimization can be refined and better adapted to the specific case (or beamline) and we present in the following a method to optimize the beam walk for a given θ range.

Firstly, we will assume that the offset angle α and $2n_{max}\alpha$ is small, thus the small-angle approximation holds, that is $\cos 2n\alpha \cong 1$ and $\sin 2n\alpha \cong 2n\alpha$ for $n = \{-n_{max}, \ldots, n_{max}\}$. The beam walk for two given energies (or angles, θ and θ_1) can then be expressed as

$$bw_{\theta,\theta_1} \cong 2|n|\alpha\left|x_{ce,\theta} - x_{ce,\theta_1}\right|, \tag{5}$$

and for simplicity we will assume that $\theta > \theta_1$.

The $x_{ce,\theta}$ function is continuous and presents only one maximum,

$$x_{ce,max} = -\left(SO^2 - OA^2\right)^{1/2}, \tag{6}$$

at $\theta_m = \arccos(OA/SO)$ if $OA < SO$. In this case the beam walk then either presents a maximum at $\theta_m = \arccos(OA/SO)$, if θ_m is in the angular range of interest (or energy range), or it is just an increasing function of θ. In all other cases, when $OA \geq SO$, $x_{ce,\theta}$ decreases with θ which means that the beam walk increases with θ (assuming that $\theta > \theta_1$). The minimization of the beam walk over the θ range can be achieved by imposing that $\mathbf{rIn}_{\theta o}$ and $\mathbf{rIn}_{\theta f}$ coincide at the same point. This implies that the centre of the Rowland circle at the minimum and maximum energy, $C_{\theta o,f}$, must have the same distance to the two extreme sample positions $S_{\theta o}$, $S_{\theta f}$, or, what is the same, $C_{\theta o,f}$ is bisecting the triangle $S_{\theta o}OS_{\theta f}$. This completely defines the set-up (see Fig. 5*a*) since, for a given θ range, OA and SO are no longer independent parameters but must fulfil the following condition,

$$OA_{opt} = SO\left[\cos\left(\frac{\theta_f + \theta_o}{2}\right) \Big/ \cos\left(\frac{\theta_f - \theta_o}{2}\right)\right]. \tag{7}$$

Figs. 5(*a*), 5(*b*), 5(*c*) and 5(*d*) show the different cases where (*a*) OA is the optimized value, (*b*) $OA = SO$, (*c*) $OA > SO$, and (*d*) $OA < SO$. The beam walks are shown in the central insert of Fig. 5.

2.3. ALBA MAD26 general description

According to the design concept explained above, the final choice of the parameters used depends on the following considerations:

(i) Geometrical restrictions at the endstation such as the height of the beam above ground define the total available length for the detector system.

(ii) The dimensions of the beam cross section and energy range define the crystal length.

(iii) The offset angle between the crystals should ideally be as small as possible; it is mostly defined by the diameter of the scintillation counters and the space needed to install a crystal.

(iv) The spacing between the crystals in the crystal fan should be sufficient to allow easy installation and replacement.

(v) The total number of crystals should be maximal but still assuring a compact and light design; since the mechanical requirements become more and more stringent for the outer crystals, their number is also limited by practicable machining tolerances.

All these parameters have been considered in the actual layout taking into account the energy range of the beamline of 8–50 keV and the geometrical restrictions of the endstation. The parameters are given in Table 1.

The optimization of the beam walk in the MAD26 design gives a beam walk maximum value of 4 mm *versus* 9 mm for the non-optimized case where $SO = OA$. Fig. 7 shows beam

Table 1
Main design parameters for the ALBA MAD26.

SO	550 mm
OA	541.12 mm
α	1.5°
Virtual source-to-detector distance	750 mm
Energy range	8–50 keV
Total number of Si 111 crystals	13
Total number of Si 220 crystals	13
Photon-counting detectors separation	20 mm
Active area of detector	11 mm diameter (circular)
Bragg angle range of Si 111 crystal	$2.27^\circ \leq \theta \leq 14.31^\circ$

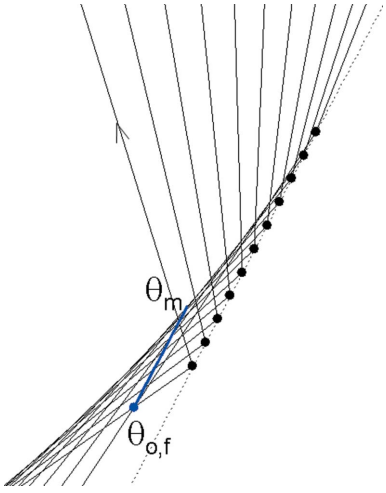

Figure 7
Propagation of the beam impact (black dots) on the outmost crystal (dotted line) for different energies. The blue dot indicates the common impact if the crystal is shifted to a position according to the blue line (optimized position of the crystal surface). One can see that the beam walk is shorter in the optimized case. Owing to the fan-like construction the crystal surfaces (optimized and non-optimized) are not exactly parallel.

and impact points (continuous black lines and black dots) on the outmost crystal for 11 θ values in the working angular range for the non-optimized case where $SO = OA$ (crystal surface represented by the dashed black line). The blue dot corresponds to the intersection of the incident beams at maximum and minimum angle, which is the impinging point for the optimized model. The blue line corresponds to the beam walk on a crystal with the same offset angle as the one mentioned above but shifted into the beam intersection according to the optimized model.

The MAD26 has two sets of crystals, one set of 13 Si 111 and a second one of 13 Si 220 that can be manually interchanged perpendicular to the beam with the help of a precision manual stage. Although changing to the Si 220 crystals will reduce the reflected intensity, it will also, especially at higher energies, increase the Bragg angle and, as a result, imprecision in manufacturing has a reduced impact on performance. With this, the user will be able to adapt for different energy ranges and compensate *de facto* inaccuracies in the mechanical set-up. As a side effect, the intrinsic resolution of the system is improved and suppression of high harmonics is increased.

3. Design materialization

A central requirement of MAD designs is that they should perform over a wide energy range (with corresponding wide angular range). To implement this, careful ray tracing is required to ensure that the beam footprint remains on the crystal at all times and that the beam is not clipped at any point. In addition, cross-talk between channels should be minimized as far as is practicable. For MAD designs operating at high energies (with corresponding low angles of incidence) this becomes particularly important as the margin for error is much reduced.

To analyse this, an error budget approach has been taken. Error budgets are commonly used in the design of accelerator systems to assess the machining and alignment requirements for the magnets (Lestrade, 2004; Wei *et al.*, 1999). This is necessary as these requirements are often at the very limit of what is technically possible. Although this is not the case with the MAD design, the same philosophy of breaking down the various sources and effects of different errors is very helpful in determining the manufacturing and assembly requirements of the system. A simplified version of the error analysis will be used, in that the various errors will be summed linearly rather than using a statistical approach. This is acceptable in this case as the uncertainty associated with the various errors is quite small and the intent is to gain a qualitative assessment of the importance of the various errors, rather than a definitive quantitative value.

The slits between the sample and the crystals should be as small as possible, to prevent stray scatter reaching the crystals and detectors, while large enough to allow all desirable rays through without clipping. The nominal upper beam size for this design is 1 mm, centred at an angle of $n\alpha$ for $n = \{-n_{\max}, \ldots, n_{\max}\}$.

However, owing to the mis-cut of the crystal and the mechanical misalignment, the beam satisfying the Bragg condition will be somewhere between $n\alpha + \varepsilon_t$ and $n\alpha - \varepsilon_t$, where ε_t is the total crystal plane error that corresponds to the sum of those errors, $\varepsilon_t = \varepsilon_o + \varepsilon_m$, where ε_m corresponds to the mechanical misalignment error and ε_o is the mis-cut of the crystals' plane.

For the design described in this paper, the angle error has been estimated at $\pm 0.023^\circ$ (see Table 2). This means that, for the slits positioned at a distance *SS* from the sample, the minimum width allowable for the slits is

$$\text{Slit width}_{\min} = \text{bs} + 2SS \sin \varepsilon_t, \tag{8}$$

where *SS* corresponds to the sample-to-slit distance and bs is the beam size.

The upper limit on slit size is set by the requirement that rays from the sample should not be able to pass the crystal. However, there needs to be some overlap between the slit edges and the crystal edges to allow for errors in the positioning of the crystal surface and still ensure complete blocking of all undesirable rays. The length of crystal that can be illuminated (usable crystal uc) is therefore set at

Table 2
Design parameters, error breakdown with values tolerated by the design, error budgets and required slit dimensions.

The dimensions are given in millimetres and the angles in degrees.

Design parameters								
Minimum angle, θ_o			Si 111 2.266° (50 keV)		Si 220 3.702° (50 keV)		Si 220 2.5° (74 keV)	
Beam size, bs			1.0		1.0		1.0	
Crystal length, cl			74		74		74	
Illuminated fraction, if			0.8		0.8		0.8	
Usable crystal length, uc			59.2		59.2		59.2	
Detector to virtual source distance, *DD*			750		750		750	
First slit to sample distance, *SS*			480		480		480	
Crystal stage axis to sample distance, *SO*			550		550		550	
Crystal planes cut error, ε_o			0.02		0.02		0.02	
Mechanical alignment error, ε_m			0.003		0.013		0.013	
Total crystal plane error, ε_t			0.023		0.033		0.033	
Slit size$_{max}$			2.04		3.34		2.25	
Slit size$_{min}$			1.39		1.55		1.55	
Nominal size of upstream slits			1.71		2.44		1.90	
Error budget breakdown								
Error budget for upstream slits = (Slit edge zone)/2			0.163		0.448		0.175	
Error component	Weight	Factor	Error budget portion (±)	Tolerance (±) on part or dimension	Error budget portion (±)	Tolerance (±) on part or dimension	Error budget portion (±)	Tolerance (±) on part or dimension
Sample to θ-axis distance (*SO*)†	0.1	6.31	0.016	0.101	0.045	0.284	0.018	0.114
Position of the slit edges (includes manufacturing)	0.9	1.00	0.147	0.147	0.403	0.403	0.158	0.158
Error budget for crystal position = $1/2(\mathrm{cl} - \mathrm{uc})\sin\theta_o$			0.293		0.478		0.323	
Error component	Weight	Factor	Error budget portion (±)	Tolerance (±) on part or dimension	Error budget portion (±)	Tolerance (±) on part or dimension	Error budget portion (±)	Tolerance (±) on part or dimension
Crystal length	0.05	$1/\sin\theta_o$	0.015	0.370	0.024	0.370	0.016	0.370
Position of central crystal to θ axis	0.45	1	0.132	0.132	0.215	0.215	0.145	0.145
Crystal mounting	0.25	1	0.073	0.073	0.119	0.119	0.081	0.081
Crystal mount to crystal center mount position	0.25	1	0.073	0.073	0.119	0.119	0.081	0.081
Error budget for detector slits								
I: total displacement of the beam at detectors owing to crystal plane error = $2DD\sin\varepsilon_t$			0.60		0.86		0.86	
II: total displacement of the beam at detectors owing to crystal surface offset = 2(error budget for crystal position)$(\sin 2\varepsilon_t/\sin\varepsilon_t)$			1.17		1.91		1.29	
III: position of 2θ relative to θ axis‡			0.25		0.25		0.25	
IV: position of the slit edges (includes manufacturing)‡			0.25		0.25		0.25	
Nominal size of detector slits = I + II + III + IV + bs			3.3		4.3		3.7	

† The factor for this component only applies to the outermost crystals, where factor = $1/\tan(n_{max}\alpha)$. ‡ These values are assumed rather than calculated. See main text for explanation.

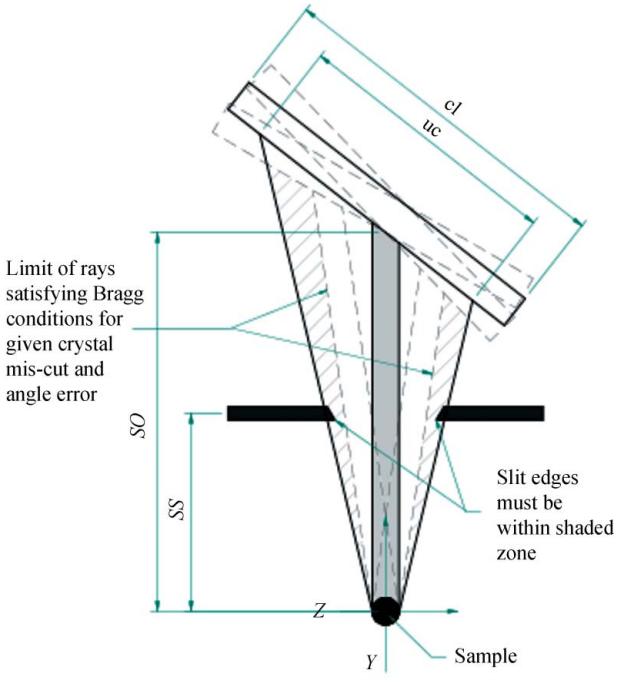

Figure 8
Diagram representing the error budget for upstream slits positioning. The crystal is represented as a rectangle, the sample as a black circle, and the slit size is defined by the slit edges. The various distances, cl, uc, *SO* and *SS* are shown as well as the *Y* and *Z* axes. The shadowed zone is defined in the text, and the limiting beams are shown as a reference.

$$\text{uc} = \text{cl} \times \text{if}, \tag{9}$$

where cl is the crystal length and if is the illuminated fraction. The slits should be designed for the worst case (smallest Bragg angle, θ_o), so projecting the illuminated area of the crystal back to the upstream slit surface gives

$$\text{Slit width}_{\max} = \text{uc} \sin\theta_o\,(SS/SO), \tag{10}$$

where *SO* is the distance from the sample to the θ-stage axis. Diagrammatically, the various boundaries are shown in Fig. 8. For the design to operate successfully, the slit edges must fall within the shaded zone between width maximum and width minimum. The size of this zone for each slit edge is

$$\text{Slit edge zone} = (\text{Slit width}_{\max} - \text{Slit width}_{\min})/2, \tag{11}$$

and the nominal size of each slit is

$$\text{Slit size} = (\text{Slit width}_{\max} + \text{Slit width}_{\min})/2. \tag{12}$$

It is conventional for engineering dimensions to be shown as a nominal figure plus or minus a certain amount. Ideally each slit edge should be in the centre of the slit edge zone, therefore the allowable error on the position of each slit edge is

$$\text{Slit edge error} = \text{Slit edge zone}/2. \tag{13}$$

This error 'budget' can then be apportioned to the various contributors with a view to finding the best compromise between performance and manufacturing cost.

For this design, the slits cannot be adjusted individually but consist of a common comb-like plate that is positioned as a single unit. Contributors to the position of the slit edges are therefore the variation in size of the slits, the variation in spacing between the slits, the variation in position of the slit plate as a whole, and the variation of the distance between the sample and the θ stage. The latter has an impact as it effectively changes the required pitch of the slits by changing the nominal angle between the crystals.

The proportion of the error budget allocated to each contributor is given by the weight column. The sum of all the weights for a given error budget must equal 1. The error budget is calculated and subdivided in the *YZ* plane (refer to Fig. 8, with *Y* in beam direction) but the dimensional tolerance relating to this error component may occur in a direction other than *Z*. The 'Factor' column in the table is thus the proportional difference between the error component in the direction in which it takes effect and the component projected into the *YZ* plane.

The size and pitch of the slits in the slit plate can be closely controlled in manufacturing; tolerances of less than 0.025 mm would not be unreasonable. Therefore the bulk of the tolerance goes towards the positioning of the slit plate and the sample–θ-axis variation. The proportion of the available error allocated to each contributor can be adjusted until reasonable values are found for all sub-errors. From Table 2 it can be seen that a 10/90 split between axis distance error and slit edge error gives good results.

The position of the crystals is now determined by the requirement that their extreme edges cannot intrude into the illuminated zone mentioned earlier. This can happen if the crystals are shorter than nominal or if they are not positioned correctly on their holders. If they do, there is a chance for rays to pass the edge of the crystal and cause background noise at the detectors. For consistency of analysis, the allowable error is projected into a plane parallel to the upstream slits and then sub-divided amongst the contributors as before. Adjusting the various weight split of the errors allows reasonable results for all error components.

A similar analysis is carried out for the slits in front of the detectors. This is simpler as it only requires the calculation of the minimum slit size required so that all desirable rays strike the detector face. The contributors to this are the movement and offset of the beam owing to the position variation of the crystal face and the tolerance on the size and position of the slits. Because there is no upper limit on the slit size, the θ–2θ error and the slit edge error are not bounded. Therefore they are estimated, based on manufacturing knowledge, and the size of the slits inferred as a result. The effect of the translation of the detectors required at different energies is not included in this analysis as the error on this motion is extremely small compared with the other errors. Indeed, given the small beam walk associated with the optimized crystal layout, it may be possible to design a MAD that does away with the linear translation of the detectors, provided their response is suitably uniform across their working aperture.

Table 2 shows the various errors and how they are derived. The last section of the table, 'Error budget for detector slits', gives the calculated slit size at the detector and the main contributing aspects. The calculations shown in the table work under the following assumptions:

(i) The crystal cut error, ε_o, is $\pm 0.02^\circ$ (guaranteed by the manufacturer).

(ii) The design of the detector is such that a pair of Si 111 and Si 220 crystals is glued to a common crystal holder. The optical surfaces of the two crystals can be adjusted manually to the desired pitch angle with a tolerance of $\pm 0.003^\circ$, ε_m. *De facto* the alignment is made with respect to the Si 111 crystal which has tighter requirements at low angles. This leads to a total angular error, ε, on the support of $\pm 0.023^\circ$.

(iii) The second crystal on the common holder, Si 220, suffers a larger pitch error than Si 111 because the crystal holder adjustment is made with respect to Si 111, and the error introduced by gluing the crystal cannot be compensated in the alignment. From experience the gluing error for the second crystal is estimated to $\pm 0.01^\circ$.

(iv) The maximum total error of the Si 220 crystal is given by the relative mounting accuracy of both crystals on the holder ($\pm 0.01^\circ$) plus the mis-cut error ($\pm 0.02^\circ$) plus the tolerance in the alignment of the holder ($\pm 0.003^\circ$). The maximum pitch deviation of the second crystal then amounts to approximately $\pm 0.033^\circ$ (as shown in Table 2).

(v) The manufacturing tolerances given in Table 2 are consistent with readily available high-quality manufacturing processes.

(vi) The 'out of plane error' (roll of the crystal) is not relevant owing to the small angles.

Assumptions (i) and (v) are guaranteed by the manufacturing process. Assumptions (ii)–(iv) have been validated with measurements performed on a prototype crystal holder that will be described in a forthcoming publication (Peral *et al.*, 2011).

The final combination of slit sizes and energy ranges depends on the errors that can ultimately be achieved with the whole assembly. Obviously the more care that is taken to minimize all errors the better.

The slit sizes chosen cover the energy range 8–50 keV with Si 111, assuming the required manufacturing and assembly tolerances are achieved. The second set of crystals has two purposes: it allows higher energies to be reached for the same manufacturing requirements, and/or achieves the same energies as Si 111 with much relaxed manufacturing requirements. This becomes clear by comparing all three columns in Table 2: Si 111 (50 keV), Si 220 (50 keV) and Si 220 (74 keV). The final mechanical design is based on the tolerances given in the first column (Si 111, 50 keV), and a three-dimensional model of the detector can be seen in Fig. 9.

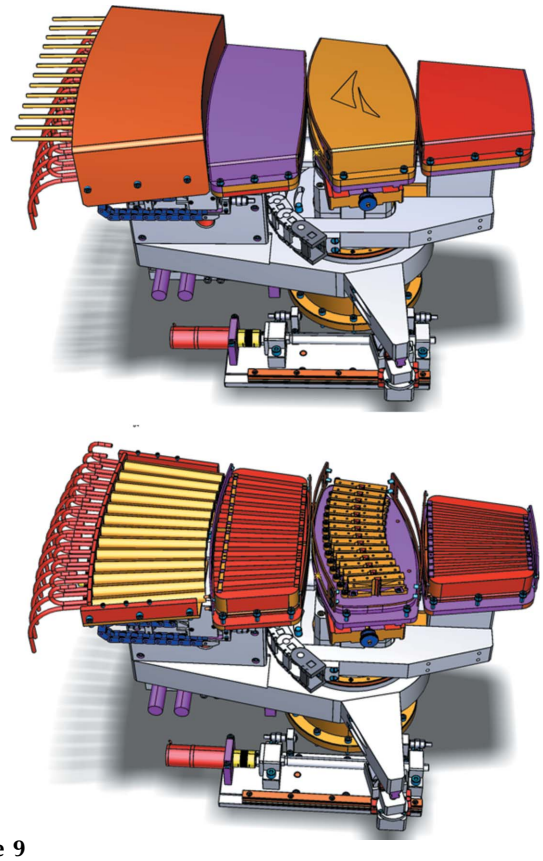

Figure 9
Three-dimensional drawing of the MAD26 design with and without the top casing.

4. Conclusions

The geometrical design of MADs has been reviewed and explained using the Rowland circle focusing geometry. This description has proven to be a valuable tool for understanding the basic principle as well as to construct and adapt MAD designs for mainly two reasons: (i) existing designs can be described, and (ii) in the case of wide-energy MADs a method can be deduced to minimize the beam walk on the analyser crystals in the energy range of interest. The MAD design of the powder diffraction beamline at ALBA has been constructed following this concept; the design criteria and relevant parameters are discussed. Since optical and mechanical errors have a large impact on the efficiency of the system, an error budget approach has been worked out to demonstrate the influence of the individual errors on the actual beam path. The resulting values in this error budget are consistent with achievable tolerances as well as with requirements on the detector system to operate over the whole energy range. Dimensions for slits, crystals and collimators, as well as mechanical tolerances, were directly introduced into the manufacturing process. The error propagation has been calculated to assure that the design will perform well under working conditions.

The authors wish to thank the beamline scientists and supporting staff of ID31, SNBL, BM16, BM25 (all at the ESRF) and I11 (Diamond); especially to German Castro, Herman Emerich, Francois Fauth, Andy Fitch and Chiu Tang for their fruitful discussions and valuable suggestions. Llibert Ribo assisted on the final realisation of the design. IP is supported by the Ramón y Cajal Program from the Spanish 'Ministerio de Ciencia e Innovación'.

References

Caciuffo, R., Melone, S., Rustichelli, F. & Boeuf, A. (1987). *Phys. Rep.* **152**, 1–71.

Cox, D. E. (1992). *Synchrotron Radiation Crystallography*, edited by P. Coppens, ch. 9, pp. 186–254. New York: Academic Press.
Hastings, J. B., Thomlinson, W. & Cox, D. E. (1984). *J. Appl. Cryst.* **17**, 85–95.
Hodeau, J. L., Bordet, P., Anne, M., Prat, A., Fitch, A. N., Dooryhée, E., Vaughan, G. & Freund, A. (1998). *Proc. SPIE*, **3448**, 353–361.
Johansson, T. (1933). *Z. Phys.* **82**, 507.
Lee, P. L., Shu, D., Ramanathan, M., Preissner, C., Wang, J., Beno, M. A., Von Dreele, R. B., Ribaud, L., Kurtz, C., Antao, S. M., Jiao, X. & Toby, B. H. (2008). *J. Synchrotron Rad.* **15**, 427–432.
Lestrade, A. (2004). *Proceedings of the 8th International Workshop on Accelerator Alignment (IWAA 2004)*, Geneva, Switzerland.
Parker, J. E., Thompson, S. P., Cobb, T. M., Yuan, F., Potter, J., Lennie, A. R., Alexander, S., Tighe, C. J., Darr, J. A., Cockcroft, J. C. & Tang, C. C. (2011). *J. Appl. Cryst.* **44**, 102–110.
Parrish, W. & Hart, M. (1985). *Trans. Am. Crystallogr. Assoc.* **21**, 51–55.
Parrish, W. & Hart, M. (1987). *Z. Kristallogr.* **179**, 161–173.
Peral, I., Ribo, L., Nicolas, J., Knapp, M. & Ferrer, S. (2011). In preparation.
Rowland, H. A. (1902). *The Physical Paper of Henry August Rowland*, pp. 487–504. Baltimore: Johns Hopkins Press.
Tartoni, N., Thompson, S. P., Tang, C. C., Willis, B. L., Derbyshire, G. E., Wright, A. G., Jaye, S. C., Homer, J. M., Pizzey, J. D. & Bell, A. M. T. (2008). *J. Synchrotron Rad.* **15**, 43–49.
Thompson, S. P., Parker, J. E., Potter, J., Hill, T. P., Birt, A., Cobb, T. M., Yuan, F. & Tang, C. C. (2009). *Rev. Sci. Instrum.* **80**, 075107.
Toraya, H. (2009). *J. Appl. Cryst.* **42**, 485–489.
Toraya, H., Hibino, H. & Ohsumi, K. (1996). *J. Synchrotron Rad.* **3**, 75–83.
Wei, F. Q., Dreyer, K., Fehlmann, U., Pochon, J. L. & Wrulich, A. (1999). *Proceedings of the 6th International Workshop on Accelerator Alignment (IWWAA1999)*, Grenoble, France.
Weisstein, E. W. (2003). *CRC Concise Encyclopedia of Mathematics*, 2nd ed., pp. 441–442. New York: Chapman and Hall/CRC.
Witz, J. (1969). *Acta Cryst.* A**25**, 30–42.